7330–7341 *Nucleic Acids Research, 2023, Vol. 51, No. 14* *Published online 13 June 2023*
https://doi.org/10.1093/nar/gkad508

Activity, substrate preference and structure of the *Hs*MCM8/9 helicase

David R. McKinzey [1,†], Chuxuan Li [2,†], Yang Gao [2] and Michael A. Trakselis [1,*]

[1]Department of Chemistry and Biochemistry, Baylor University, Waco, TX 76706, USA and [2]Department of Biosciences, Rice University, Houston, TX 77005, USA

Received April 25, 2023; Revised May 25, 2023; Editorial Decision May 26, 2023; Accepted May 31, 2023

ABSTRACT

The minichromosomal maintenance proteins, MCM8 and MCM9, are more recent evolutionary additions to the MCM family, only cooccurring in selected higher eukaryotes. Mutations in these genes are directly linked to ovarian insufficiency, infertility, and several cancers. MCM8/9 appears to have ancillary roles in fork progression and recombination of broken replication forks. However, the biochemical activity, specificities and structures have not been adequately illustrated, making mechanistic determination difficult. Here, we show that human MCM8/9 (*Hs*MCM8/9) is an ATP dependent DNA helicase that unwinds fork DNA substrates with a 3′–5′ polarity. High affinity ssDNA binding occurs in the presence of nucleoside triphosphates, while ATP hydrolysis weakens the interaction with DNA. The cryo-EM structure of the *Hs*MCM8/9 heterohexamer was solved at 4.3 Å revealing a trimer of heterodimer configuration with two types of interfacial AAA$^+$ nucleotide binding sites that become more organized upon binding ADP. Local refinements of the N or C-terminal domains (NTD or CTD) improved the resolution to 3.9 or 4.1 Å, respectively, and shows a large displacement in the CTD. Changes in AAA$^+$ CTD upon nucleotide binding and a large swing between the NTD and CTD likely implies that MCM8/9 utilizes a sequential subunit translocation mechanism for DNA unwinding.

GRAPHICAL ABSTRACT

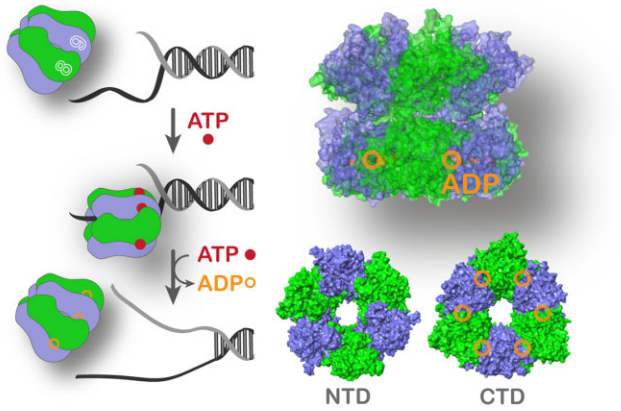

INTRODUCTION

MCM8 and MCM9 belong to a conserved family of minichromosomal maintenance (MCM) proteins that include the replicative eukaryotic MCM2–7 and the archaeal MCM helicases (Supplementary Figure S1). MCM proteins are all comprised of the N-terminal domains (NTD) and the C-terminal AAA$^+$ ATPase domains (CTD). The CTD contains the canonical Walker A (WA) motif to localize binding of nucleoside triphosphates (NTPs), the Walker B (WB) motif to hydrolyze NTPs, and two DNA binding loops for DNA translocation (Figure 1A) (1,2). The NTD includes DNA binding hairpin loops and a zinc finger (ZF) motif which allows for tight binding of DNA (3). MCM proteins form hexamers; either heterohexamers for MCM2–7 or homohexamers for the archaeal MCM (4,5). MCM8 and MCM9 have been shown to directly interact and form a stable trimer of heterodimers, but they do not appear to exchange or directly interact with MCM2–7 (6). Unlike the replicative MCM2–7 helicase, MCM8 and 9 (MCM8/9) only occur together in higher eukaryotes such as humans but are absent in commonly studied organisms such as *C. elegans*, *S. cerevisiae* and Drosophila (7–11).

Mutation of MCM8 leads to infertility in women, characterized by signs of primary ovarian insufficiency (POI)

*To whom correspondence should be addressed. Tel: +1 254 710 2581; Email: michael_trakselis@baylor.edu
†The authors wish it to be known that, in their opinion, the first two authors should be regarded as Joint First Authors.

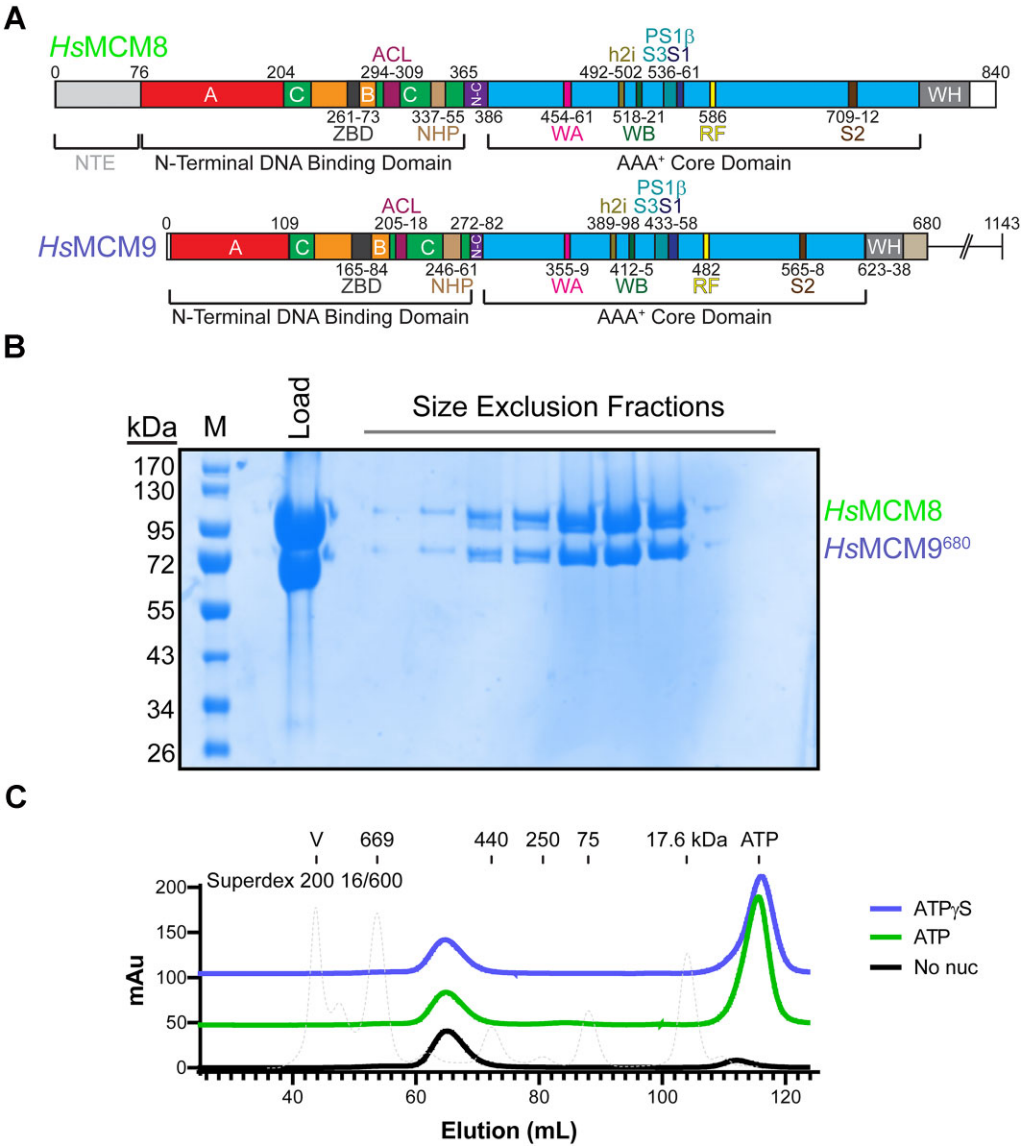

Figure 1. Schematic, purification, and oligomeric state the *Hs*MCM8/9^{680} complex. (**A**) Schematic of *Hs*MCM8 and *Hs*MCM9 containing the N-terminal DNA binding domain (NTD) and a C-terminal AAA$^+$ domain (CTD) with conserved motifs: ACL – allosteric connecting loop, ZBD – zinc binding domain, NHP – N-terminal hairpin, N–C NTD to CTD linker, WA – Walker A, h2i – helix 2 insertion, WB – Walker B, S3 – sensor 3, PS1β – presensor 1 beta hairpin, RF – arginine finger, S2 – sensor 2, WH – winged helix. *Hs*MCM8 also contains a limited N-terminal extension (NTE) from 1–76 amino acids, while *Hs*MCM9 contains a long C-terminal extension (CTE) from 680 to 1143 amino acids. (**B**) Representative SDS-PAGE gel after (**C**) Gel filtration on a Superdex 200 16/600 column showing purity and 1:1 complex of MCM8/9^{680} either with no nucleotide (black), ATP (green), or ATP**γ**S (blue). A dashed line indicates the elution of the MW standards with indicated size at the top of the plot.

such as early menopause, amenorrhea and small or absent ovaries (12–16). Recent studies have shown a similar phenotype in men deficient for MCM8 that include azoospermia (17). Unsurprisingly, mutations in MCM9 also show phenotypical characteristics of POI that include delayed puberty and short stature. Cells with defective MCM8/9 are sensitive to crosslinking agents such as mitomycin C and cisplatin (14,18). A link between various cancers and mutations of MCM8/9 have also been observed, including sex-specific (ovarian and testicular), liver, and colon cancers. MCM8/9 has several interaction partners, including RAD51, the MRN complex (MRE11–RAD50–NBS1), mismatch repair proteins (MSH2, MSH3, MLH1, PMS1) and the clamp–loader (RFC) (6,19–21). Cellular assays show that MCM8/9 acts to facilitate replication fork progression, stabilize stalled forks, and initiate downstream homologous recombination (HR) processes from broken replication forks, prior to RAD51 binding (19,21). Therefore, the role of MCM8/9 seems diverse and complex, appearing in multiple genomic maintenance pathways. Importantly, inhibition of MCM8/9 is deemed a viable strategy in combination with other chemosensitizers as a novel chemotherapy approach (22).

The enzymatic activity, cellular functions and structural characteristics of the MCM8/9 complex need to be carefully examined. Previous studies of the MCM8/9 complex

have shown some limited DNA binding and unwinding activity, but the substrate specificity was not explored (23–25). Up to now, structural studies have only revealed high resolution data for the NTD of the MCM8/9 hexamer, whereas the CTD has only been solved at low resolution in the absence of nucleotide ligands (26). In this study, we have determined DNA binding preferences and affinities, conditions for human MCM8/9 (*Hs*MCM8/9) loading onto and unwinding of DNA, translocation polarity and the kinetics of DNA stimulated ATP hydrolysis. Moreover, we obtained the heterohexameric cryo-EM structure of the human MCM8/9 complex bound to ADP at 4.3 Å that includes local refinement of the NTD and CTD at 4.1 and 3.9 Å, respectively. Altogether, we provide a comprehensive and quantitative biochemical and structural characterization of the *Hs*MCM8/9 helicase complex.

MATERIALS AND METHODS

Materials

Oligonucleotides were purchased HPLC purified from Sigma (St. Louis, MO) or IDT (Coralville, IA) and listed in Supplementary Table S1. The plasmid, pFastBac dual, was a generous gift from Jung-Hyun Min (Baylor University). All other chemicals were analytical grade or better.

Cloning of MCM8 and 9 constructs

The human MCM9 gene was amplified from pEGFPc2-MCM9 to either full length or truncated to the first 680 amino acids and adding a N-terminal 6 × His tag (13). MCM9 full-length or 680 truncation was digested with *XhoI*/*NsiI* and ligated into pFastBac dual under the p10 promoter. Human MCM8 was cloned similarly using *StuI*/*NotI* and adding on a N-terminal StrepII tag followed by a TEV protease cleavage site into the polyhedron (PH) promoter. Site directed mutagenesis of the resulting plasmid was carried out using Platinum SuperFi II (Thermo Fisher, Waltham, MA) to create the Walker B mutants for MCM8 (E519Q) and MCM9 (E415Q). Plasmids were verified by whole plasmid sequencing (Plasmidsaurus, Eugene, OR). The resulting constructs were transposed into modified DH10Bac cells (Thermo Fisher, Waltham, MA) using pKD46 lambda red recombination to remove the *chiA*/*cath-v* genes while adding chloramphenicol (Chl) resistance and eGFP under the polyhedrin promoter.

Baculovirus production

Baculovirus was produced using the single step method (27). Briefly, SF9 cells were split to 0.75 × 10^6 cells/ml and allowed to recover for 3–4 h. Recombinant bacmid was transfected into the cells using a 1:2 ratio DNA to 40k LPEI (Polysciences, Warrington, PA). P0 virus was harvested five days post transfection and used at a 1:3000 dilution to infect SF9 cells for P1 production. Virus containing media was stored at 4°C.

Protein expression and purification

Protein expression was performed as described (27). Tni cells (Expression Systems, Davis, CA) were seeded into 1200 ml of ESF921 to a density of 1 × 10^6 cells/ml and then infected with P0 or P1 at a 1:100 dilution virus to culture. The culture was split into two 2.8 l flasks and placed into a 25°C incubator at 115 rpm shaking for 86–90 h. Cells were then harvested at 3000 × g for 15 min. The resulting cell paste was resuspended and washed with PBS containing 1 mM PMSF and then harvested again at 3000 × g for 15 min. The cell paste was then flash frozen and kept at -80°C until purification. 10 mL of cell paste was resuspended in 100 ml of lysis buffer containing 50 mM Tris–HCl (pH 8), 300 mM NaCl, 50 mM Na-Glutamate, 50 mM arginine, 10% glycerol, 1 mM EDTA, 1 mM TCEP, 1 mM PMSF, 5 μg/ml leupeptin and 5 μg/ml pepstatin A. Cells were lysed in an Avestin-C3 homogenizer (Ottawa, ON) using two rounds at 10 000 psi. Lysate was centrifuged at 23 000 rpm for 1 h at 4°C. Clarified lysate was filtered before injecting onto a 5 ml StrepTactin XT 4Flow (IBA, Gottingen, Germany) column attached to a AKTA Pure25 FPLC (Cytiva, Marlborough, MA). The column was washed with 10 CV of lysis buffer supplemented with 1 M NaCl and then with 5 CV of Lysis buffer with 100 mM NaCl. Proteins were eluted by a step gradient using Lysis buffer with 100 mM NaCl and 50 mM biotin. Fractions were pooled and injected onto a 5 ml HiTrap Q HP column and eluted with a linear NaCl gradient (0.1–1 M). MCM8/9 eluted around 300 mM NaCl. Fractions containing MCM8/9 were loaded onto a Superdex 200 16/60 with lysis buffer. The hexamer fractions were concentrated by first diluting the NaCl concentration to below 100 mM and then eluting the complex with a step gradient to lysis buffer contraining 300 mM NaCl using a 1 mL HiTrap Q HP column. The resulting concentrated protein was snap frozen in liquid N_2 and stored at -80°C. Mutants were expressed and purified similarly. Protein purity and size were qualitatively analyzed by SDS-PAGE.

S1 nuclease assay

S1 nuclease reactions were prepared using 500 nM MCM8/9^{680} diluted in S1/MCM8/9 reaction buffer consisting of 20 mM Bis–Tris–acetate (pH 6.5), 50 mM KOAc, 10 mM $Mg(OAc)_2$, 50 mM K-glutamate, 1 mM DTT, ± 1 mM nucleotide. 10 nM of annealed DNA substrate (Supplementary Table S1) was added to reactions and incubated on ice for 15 min. Reactions were warmed to 30°C for 2.5 min and 100 units of S1 nuclease was added. After 1 h, reactions were quenched with and equal volume of formamide/TBE/0.2%SDS/500 nM unlabeled DNA trap. DNA was denatured at 95°C for 15 min before being loaded onto a 15% urea TBE PAGE. Separation was carried out at 200 V for 1 ho in 1× TBE. Gels were imaged using a RGB Typhoon (Cytiva, Marlborough, MA). Data was analyzed using ImageQuant (v10.1) and graphs made using GraphPad prism v9.5 (San Diego, CA) showing percent of DNA digestion under conditions indicated.

DNA binding assays

Fluorescence anisotropy DNA binding measurements reactions (35 μl) were prepared by serially diluting protein in MCM8/9 reaction buffer consisting of 20 mM Tris–acetate

(pH 8), 50 mM KOAc, 10 mM $Mg(OAc)_2$, 50 mM K-glutamate, 1 mM DTT, ±0.5 mM ATPγS from 200 nM to 3.125 nM $MCM8/9^{680}$ hexamer in a 384-well plate on ice before 2.5 nM of Cy3 labeled DNA substrate (Supplementary Table S1) was added. Reactions were incubated for 15 min to allow binding. Anisotropy measurements were taken using a Tecan Spark plate reader at 25°C with excitation at 510 ± 25 nm and emission at 580 ± 20 nm. The average total change in Cy3 fluorescence across MCM8/9 concentrations was less than 12% for all substrates tested, indicating that fluorescence quenching or enhancement was not significantly affecting the anisotropy measurements. Reactions were performed in triplicate, and the K_d was calculated from the following equation:

$$Y = B_0 + \frac{B_{max}x}{K_d + x} \quad (1)$$

where B_0 is the fraction bound at 0 nM protein, B_{max} is the fraction bound at saturation, x is the protein concentration, and K_d is the dissociation constant for protein binding using GraphPad Prism. EMSA experiments were performed similarly except bound DNA was separated from unbound DNA using a 2.5% TB agarose gel electrophoresed at 250 V for 20 min. Gels were imaged using an RGB Typhoon with a Cy3 filter set.

Unwinding assays

Gel based unwinding was conducted as follows. When protein concentration was varied, $MCM8/9^{680}$ hexamer was diluted from 1000 to 100 nM in MCM8/9 reaction buffer with 0.5 mM ATPγS to which 5 nM of Cy3 (or FAM) labelled and annealed DNA substrate (Supplementary Table S1) was added. Reactions were incubated on ice for 10 min and then quickly warmed to 37°C for 2.5 min. Unwinding reactions were initiated with 5 mM ATP and 50 nM unlabeled DNA trap complementary to the unlabeled DNA strand. Reactions continued for the indicated time and then were quenched with an equal volume containing 1% SDS, 100 mM EDTA, 30% glycerol, and 1000 nM unlabeled DNA trap. To analyze unwinding, 10 μl of each reaction were separated on a 15% TBE PAGE at 200 V for 1 h. Gels were imaged using a RGB Typhoon using Cy3 filter set. Time based experiments were conducted similarly but with 500 nM protein and timepoints as indicated. Quantification of band intensity was done using Image Lab v6.1 (Bio-Rad, Hercules, CA), comparing ssDNA to dsDNA to calculate % unwinding.

ATPase assays

ATP hydrolysis rate was measured using either ^{32}P-γ-ATP TLC based or malachite green detection (Sigma, St. Louis, MO) of Pi in a plate reader format. $MCM8/9^{680}$ was diluted to indicated concentrations as noted in MCM8/9 reaction buffer. Reactions were heated to 37°C for 2.5 min and 1 mM ATP was added. For TLC-based measurements ATP, 1 mM ATP stock was spiked with ^{32}P-γ-ATP (Perkin Elmer, Waltham, MA). Time points were taken as indicated and quenched with an equal portion of 0.5 M EDTA/0.1% SDS and placed on ice. For malachite green 96-well assays, the reactions were diluted 10-fold with MilliQ water and developed per the manufacturer protocol (Sigma-Aldrich, St. Louis, MO) with absorbance measurements taken at 600 nM using a TECAN Spark microplate reader (Tecan, Morrisville, NC). For TLC based assays, 1 μl of reactions were spotted onto a LPEI-Cellulose TLC plate and allowed to dry. The plates were developed using 0.6 M KPO_4 (pH 3.5) buffer and left to dry before exposing to a phosphor screen overnight. Scans were taken using a RGB Typhoon and analysis carried using ImageQuant software.

Sample preparation

To prepare the complex of $MCM8/9^{WT}$ or $MCM8/9^{WB}$ with the fork DNA215 (Supplementary Table S1) in the presence of ATP or ATPγS, 1 mg/ml protein was incubated with the DNA with a molar ratio of 1:2 and 5 mM ATP or ATPγS in buffer containing 50 mM Tris (pH 7.7), 100 mM KCl, 10 mM K-glutamate, 3 mM DTT and 5 mM $MgCl_2$. After 20 min incubation at 25°C, the reaction mixture was centrifuged at 9000 rpm for 10 min to remove any precipitates. 3.0 μl of freshly prepared supernatant was applied onto glow-discharged Quantifoil R1.2/1.3 Quantifoil holey carbon or UltrAuFoil holey gold R1.2/1.3 grids (Quantifoil). The grid was blotted for 2 s in 100% humidity at force -3 and was plunge-frozen in liquid ethane using a Vitrobot Mark IV (FEI).

Data collection and processing

For full-length $MCM8/9^{WT}$ structural determination, 2197 micrographs of MCM8/9 complexes were collected without tilting, and 1592 micrographs were collected with 30-degree stage tilting. Both datasets were collected on a Titan Krios electron microscope operated at 300 kV (cryo-EM core facility at University of Texas McGovern Medical School) using the counting mode with a nominal magnification of 130 K (calibrated pixel size of 1.11 Å). Movies were recorded with a K2 Summit camera, with the dose rate at the detector set to 7 e^- s^{-1} $Å^{-2}$. The total exposure time for each video was 7 s, which was fractionated into 35 frames of sub-images. The defocus values ranged between 0.7 and 3 μm. MotionCor2 was used for drift-correction and electron-dose-weighting for all movies (28). The defocus values were estimated on non-dose-weighted micrographs with Gctf (29). 1 055 864 particles from untilted data and 802 617 particles from tilted data were separately subjected to 2D classification with RELION (30). 377548 particles were selected from the untilted dataset and 207588 particles were selected from tilted dataset after 2D classification. The selected particles were subjected to further 2D and 3D classification in cryoSPARC (31). Only the class showing clear secondary structures features was selected for non-uniform refinement in cryoSPARC, which produced a MCM8/9 hexamer structure at 7.4 Å. Imposing C3 symmetry to the refinement yielded a map at 6.5 Å resolution, judged by the 0.143 cutoff criterion in FSC.

For the $MCM8/9^{WB}$ complexes, 11 295 micrographs of were collected on a Titan Krios electron microscope operated at 300 kV (cryo-EM core facility at University of Texas McGovern Medical School) using the counting mode

with a nominal magnification of 130 K (calibrated pixel size of 1.11 Å). Movies were recorded with similar parameters as MCM8/9^{WT} but without stage tilting. MotionCor2 (28) and Gctf (29) were used for drift-correction and CTF estimation. 11 087 micrographs were selected for subsequent processing upon visual examination of the micrographs. 5188040 particles were picked from those 11 087 selected micrographs. After 2D and 3D classification in RELION (30), 510 158 Particles from the class with the best high-resolution features were selected for subsequent processing in cryoSPARC (31). Further 2D and 3D-classification were performed to clean the datasets and 227818 particles were selected. The 227818 particles were reextracted in RELION (30) and went through 3D refinement, CTF refinement and particle polishing. The final map of MCM8/9^{WB} at 4.3 Å with C3 symmetry was generated with non-uniform refinement in cryoSPARC (31). Local refinement of the NTD and CTD with corresponding masks generated maps of the CTD at 3.9 Å and NTD at 4.1 Å, both with C3 symmetry.

Model building and refinement

For the refinement of MCM8/9^{WB} complexes, the crystal structure of NTD (PDB ID: 7DP3 and 7DPD) and the Alphafold generated full-length MCM8/9 structures were used as initial models. Each of the protein chains were then manually docked into the cryo-EM density maps in Chimera (32). The models were first manually adjusted in COOT (33) and then refined in Phenix (34) with real-space refinement and secondary structure and geometry restraints. Statistics of all cryo-EM data collection and structure refinement are shown in Supplementary Table S2. The refined MCM8/9^{WB} complexes structure was rigid-body docked into the 6.5 Å resolution MCM8/9^{WT} complexes for structure interpretation.

RESULTS

*Hs*MCM8/9 binds ssDNA with high affinity in the presence of triphosphate nucleosides

*Hs*MCM8/9 was coexpressed and purified from insect cells; however, the full-length constructs were less stable and tended to aggregate during the purification and downstream assays. Therefore, a truncated form of MCM9 (MCM9^{680}) was created, that kept the NTD, CTD and the winged-helix (WH) domain. The remaining unstructured C-terminal extension (CTE) containing regulatory motifs for nuclear localization and protein-protein interactions (19,35) is removed (Figure 1A, B). Gel filtration analysis shows that MCM8/9^{680} forms a stable coeluting heterohexamer, either without or with preincubation of ATP or the slowly hydrolyzable ATP analogue, ATP**γ**S (Figure 1C).

The binding affinity of MCM8/9^{680} to multiple DNA substrates was examined by electrophoretic mobility shift assays (EMSA) (Figure 2A) and then quantified by fluorescence anisotropy assays (Figure 2B–G). High affinity MCM8/9^{680} binding to ssDNA (K_d = 19 ± 4 nM) was found to require ATP**γ**S (Figure 2B). In the absence of any nucleotide, the affinity decreased significantly, >20-fold (to 462 ± 43 nM). The binding of MCM8/9^{680} with ATP**γ**S to other DNA substrates, including an equal arm fork (26 ± 4 nM), 3′ Arm (12 ± 3 nM), 5′ Arm (10 ± 1 nM), and full duplex double-stranded DNA (dsDNA) (485 ± 43 nM) were also examined. Our results suggested a clear preference of MCM8/9 for any substrate containing a ssDNA region, resulting in lower K_d values compared to dsDNA (Figure 2B–G). Interestingly, the measured K_d for dsDNA is at a similar value to that for ssDNA without any NTP added.

To determine the nucleotide-dependence of MCM8/9^{680} binding to a fork DNA substrate, an S1 nuclease protection assay was conducted (Figure 2H). S1 is a ssDNA specific endonuclease and will preferentially cleave the 30-base ssDNA flap regions of the fork if MCM8/9^{680} is not stably bound. In the absence of any nucleotide, MCM8/9^{680} had only partial protection of the 3′-arm. When ATP**γ**S was included, S1 nuclease activity was almost completely blocked, indicating a very stable MCM8/9^{680}/DNA complex (Figure 2I, J). Upon inclusion of either ATP or ADP, only partial protection was observed, similar to no nucleotide. Interestingly, there was almost complete S1 nuclease protection in the presence of a mixture of dNTPs, similar to that of ATP**γ**S, but much greater than for ATP, indicating that the 2′OH is not needed to support stable ssDNA binding.

The ATPase activity of HsMCM8/9 is stimulated with addition of DNA to translocate and unwind in the 3′ to 5′ direction

To test whether the MCM8/9^{680} ATP hydrolysis rate is stimulated by ssDNA, a ^{32}P-**γ**-ATPase assay was performed. MCM8/9^{680} alone showed a basal rate of ATP hydrolysis that is stimulated significantly upon addition of ssDNA (Figure 3A, B). This result is similar to that obtained using a malachite green microplate assay, which measures phosphate release, where MCM8/9^{680} exhibits 2.7-fold stimulation of ATPase activity upon the addition of M13 ssDNA (Figure 3C, D). As dNTPs acted to stabilize binding of MCM8/9^{680} to fork DNA (Figure 2I, J), we also tested the ability to of MCM8/9^{680} to hydrolyze dNTPs. Although the phosphate release rate catalyzed by MCM8/9^{680} was stimulated with dNTPs, it was significantly lower overall than with ATP.

Although some limited DNA unwinding activity of MCM8/9 has been shown previously (23,25,26), the conditions for optimal unwinding have not been determined. The unwinding activity of MCM8/9^{680} on an equal arm fork DNA substrate with 20 base arms is maximal when $Mg(OAc)_2$ was used compared to $MgCl_2$ (Supplementary Figure S2A). Unwinding was also inhibited in the presence of the nonhydrolyzable AMP-PNP analog with either Mg salt as expected. Increasing MCM8/9^{680} concentration enhanced unwinding up until the highest concentration tested (Supplementary Figure S2B). However, the DNA unwinding activity was not robust in the simplest experimental method, and so, we sought to explore alternative strategies to increase the unwinding rate.

Based on the finding above that the γ-phosphate was required for stable binding to ssDNA (Figure 2), MCM8/9^{680}

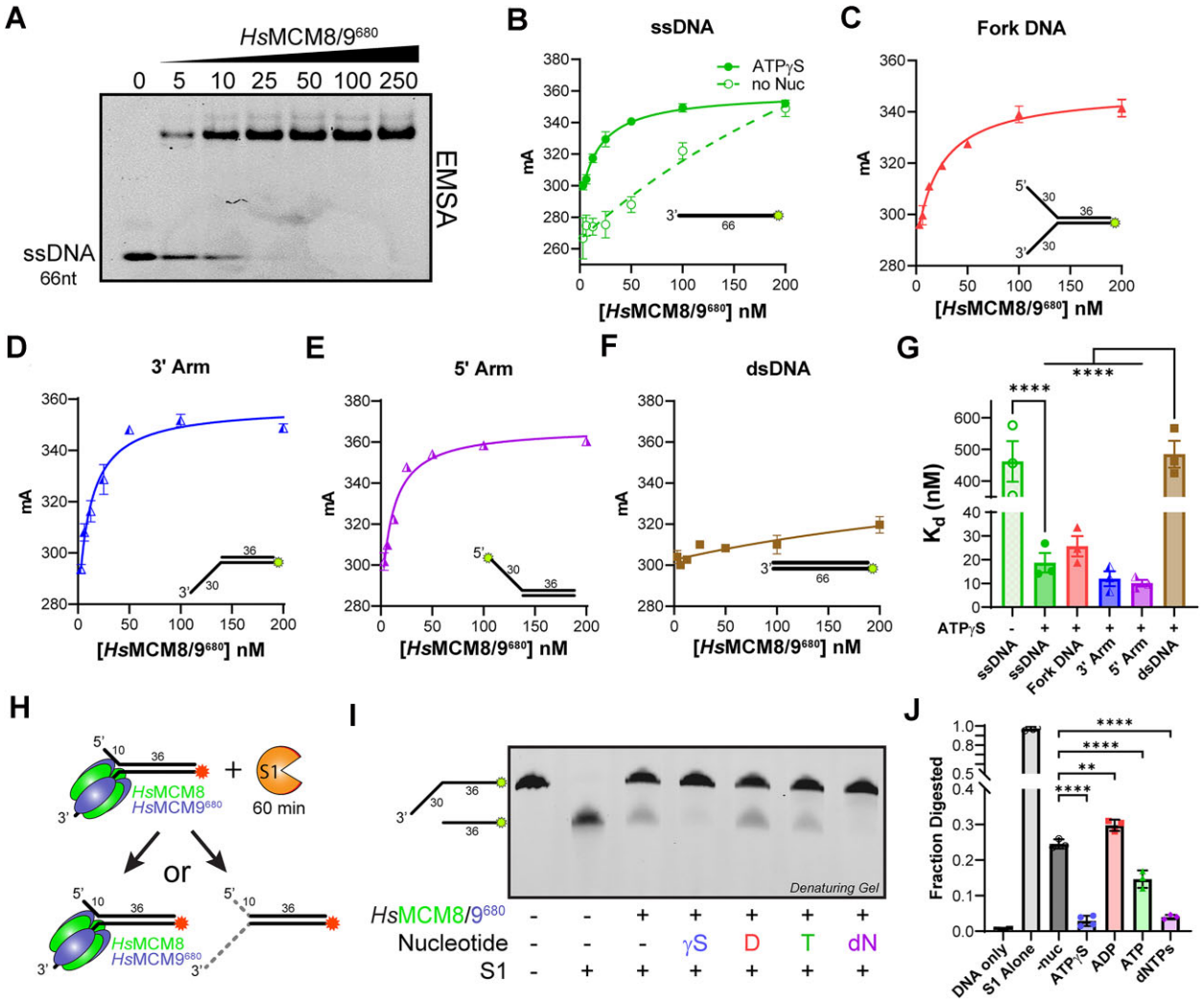

Figure 2. *Hs*MCM8/9^{680} binds with high affinity to ssDNA substrates with nucleoside triphosphates. (**A**) EMSA gel showing a shift of Cy3 labeled ssDNA substrate upon increasing concentration of *Hs*MCM8/9^{680}. (**B**–**F**) Fluorescence anisotropy values were plotted and fit to Equation 1 to extrapolate the K_d values for each substrate ssDNA (green, DNA15), Fork DNA (red, DNA14/15Cy3), 3′arm (blue, DNA19/15Cy3), 5′arm (purple, DNA218/15Cy3) and dsDNA (brown, 219/15Cy3). The Cy3 fluorophore position on each DNA substrate is indicated in the schematic. Error bars represent the standard error of the mean for at least three replicates and are within the symbols if not visible. (**G**) Comparison of K_d of binding to all substrates ± ATPγS for ssDNA and including ATPγS for all other substrates. (****$P < 0.0001$, by paired two-sided *t*-test). (**H**) Schematic of the S1 nuclease protection assay showing the degradation of ssDNA in the absence of *Hs*MCM8/9. (**I**) Representative gel showing degradation of the DNA template (DNA228/15Cy3) in the absence and presence of various nucleotides and *Hs*MCM8/9^{680}. (**J**) Quantification of fraction digested under various conditions from three independent experiments. Error bars represent the standard error of the mean (**$P < 0.01$ or ****$P < 0.0001$ by paired two-sided *t*-test).

was preincubated with a 3′ long-arm fork DNA substrate in the presence of 0.5 mM ATPγS to promote more stable loading. The reactions were then initiated with a 10-fold excess of ATP (5 mM) and an excess ssDNA trap (100 nM) complementary to the unlabeled strand. In this situation, the fraction of unwound product increased dramatically and was similar across all concentrations tested (Figure 3E, F). With this strategy, the polarity of unwinding could now be confirmed as 3′ to 5′, as the asymmetric 3′ long-arm substrate afforded four times more unwound product compared to the asymmetric 5′ long-arm substrate at 100 nM MCM8/9^{680} (Figure 3G, H). Even more complete 3′ long-arm fork unwinding is observed at higher concentrations (500 nM) of MCM8/9^{680} over a similar time course (Supplementary Figure S3).

The cryo-EM structure of HsMCM8/9 nucleotide complex

We then set out to determine the structure of MCM8/9 complex by cryo-EM. Guided by the biochemical studies, the wild-type MCM8/9^{680} (MCM8/9^{WT}) complex was assembled with ATPγS and an internal hairpin fork DNA bearing a 22 nt 3′ overhang and 10 nt 5′ overhang (DNA215, Supplementary Table S1). Despite being clearly visible on EM grids, the sample suffered from severe orientation issues with a large fraction of top-down views of the hexamers (Supplementary Figure S4). The combination of top-down views collected from untilted grids and side views collected from a 30-degree titled stage yielded a ring-shaped MCM8/9 hexamer structure at 6.5 Å with C3 symmetry (Figure 4A and Supplementary Figure S4). However, DNA

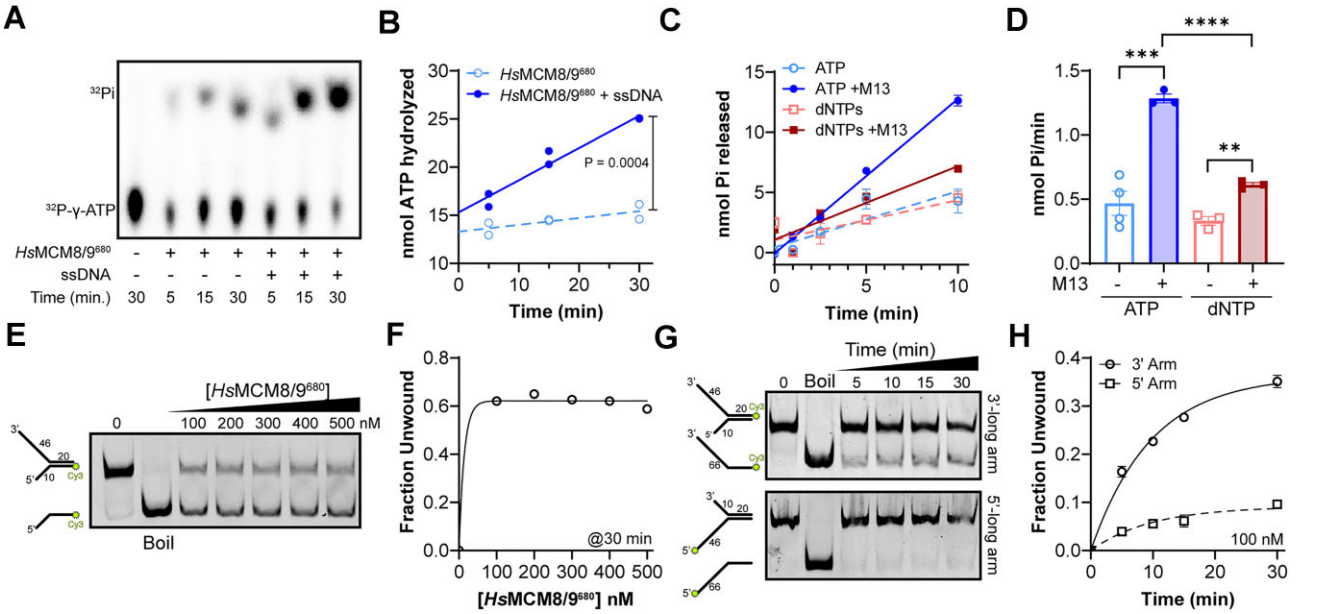

Figure 3. ssDNA stimulated ATPase activity of *Hs*MCM8/9^{680} is utilized to unwind fork DNA with 3′–5′ polarity. (**A**) Representative TLC plate showing ^{32}P-γ-ATP and ^{32}Pi with indicated conditions and (**B**) quantified in the absence (light blue, ○) or presence (blue ●) of 66mer ssDNA from two independent experiments. (**C**, **D**) A malachite green plate reader assay measured the release of Pi in the absence (open symbols, dashed) or presence (closed symbols, solid) of M13 ssDNA with either ATP (o or ●, shades of blue) or dNTPs (□ or ■, shades of red) from three-four independent experiments. Error bars represent the standard error of the mean and are within the symbol if not visible. (**E**) DNA unwinding of a 3′-long arm fork substrate (5 nM, DNA232/15Cy3) with increasing concentration of *Hs*MCM8/9^{680} (as indicated) and (**F**) quantified for fraction unwound. DNA unwinding of either a (**G**) 3′ long arm (top) or 5′ long arm (bottom, (DNA230/15Cy3) fork substrate at 100 nM *Hs*MCM89^{680} following (**H**) the fraction unwound as a function of time.

was not observed in the MCM8/9^{WT} central channel.

To further improve the resolution, single WB mutants of both MCM8 and MCM9^{680} (MCM8/9^{WB}) were purified and then complexed in the presence of the fork DNA and ATP. MCM8/9^{WB} had similar ssDNA binding affinity compared to MCM8/9^{WT}. However, MCM8/9^{WB} was more stable on fork DNA with ATP in a S1 nuclease protection assay, was unable to unwind a 3′ long arm fork DNA and had only a slight increase in ATPase activity above background with addition of M13 (Supplementary Figure S5). Therefore, WB mutations may stabilize the ternary complex by slowing down ATP hydrolysis locking the helicase in a DNA bound conformation (36).

Interestingly, the orientation issue was largely alleviated with MCM8/9^{WB} (Supplementary Figure S6). A ring-shaped hexameric MCM8/9^{WB} complex structure was determined at 4.3 Å (with C3 symmetry) (Figure 4B) but again without DNA bound. The hexameric ring has dimensions of ∼140 Å in width and ∼100 Å in height. The central channel of the ring is larger than 22 Å, potentially to accommodate both ss and dsDNA. The NTD and CTD were separately refined to 4.1 Å and 3.9 Å, respectively (Figure 4C, D and Supplementary Figure S6). Most bulky sidechains and the bound nucleotide molecules are visible at this resolution (Supplementary Figure S7). Due to the relatively low resolution of MCM8/9^{WT}, we generated an MCM8/9^{WT} model via rigid body docking individual NTD and CTD of MCM8/9^{WB} into the WT cryo-EM map. The MCM8/9^{WT} and MCM8/9^{WB} structures take similar overall conformations (Supplementary Figure S8). Minimal differences were observed between CTD when NTD are aligned for both the MCM8 and 9 monomers. MCM8/9 and MCM9/8 CTD interfaces are almost identical for MCM8/9^{WT} and MCM8/9^{WB}. Thus, the high-resolution MCM8/9^{WB} structure was used for subsequent analysis.

To examine the communication between the NTD and CTD of MCM8/9^{WB}, individual domains were aligned to the archaeal *Saccharolobus solfataricus* MCM (*Sso*MCM) structure co-crystalized with ssDNA and nucleotide (37). When the NTD of one subunit was aligned to that in *Sso*MCM (monomer A), there was a 21- or 26-degree rotation of the MCM8 and MCM9 CTD at the two interfaces, respectively (Figure 4E-F). Moreover, the CTD in MCM8 and MCM9 swung 13.3 or 18.0 Å away from its position in *Sso*MCM at the two interfaces, indicating apparent flexibility between the NTD and CTD of MCM8/9. Similar CTD movement relative to the NTD was also observed for MCM8 and MCM9 aligned with apo archaeal MCM (38), and yeast MCM2–7 complex (39) (Supplementary Figure S9).

In the MCM8/9^{WB} structure, there are six ATP binding sites located at the alternating interfaces formed by MCM8 and MCM9 (Figure 4D). Compared to the apo human MCM8/9 crystal structure (40), the presence of ADP in this structure orders several loops surrounding the ATPase sites, including MCM8 595–614, 700–709 and MCM9 460–468 and 489–499, which are observed to interact with the adenosine base (Figure 5C-D). Moreover, if the subunit bearing WA and WB motifs is aligned, the arginine finger on the other subunit moves away 5.3 and 8.4 Å, respectively, upon ADP binding at the two interfaces. We also compared our structure to *Sso*MCM co-crystalized with

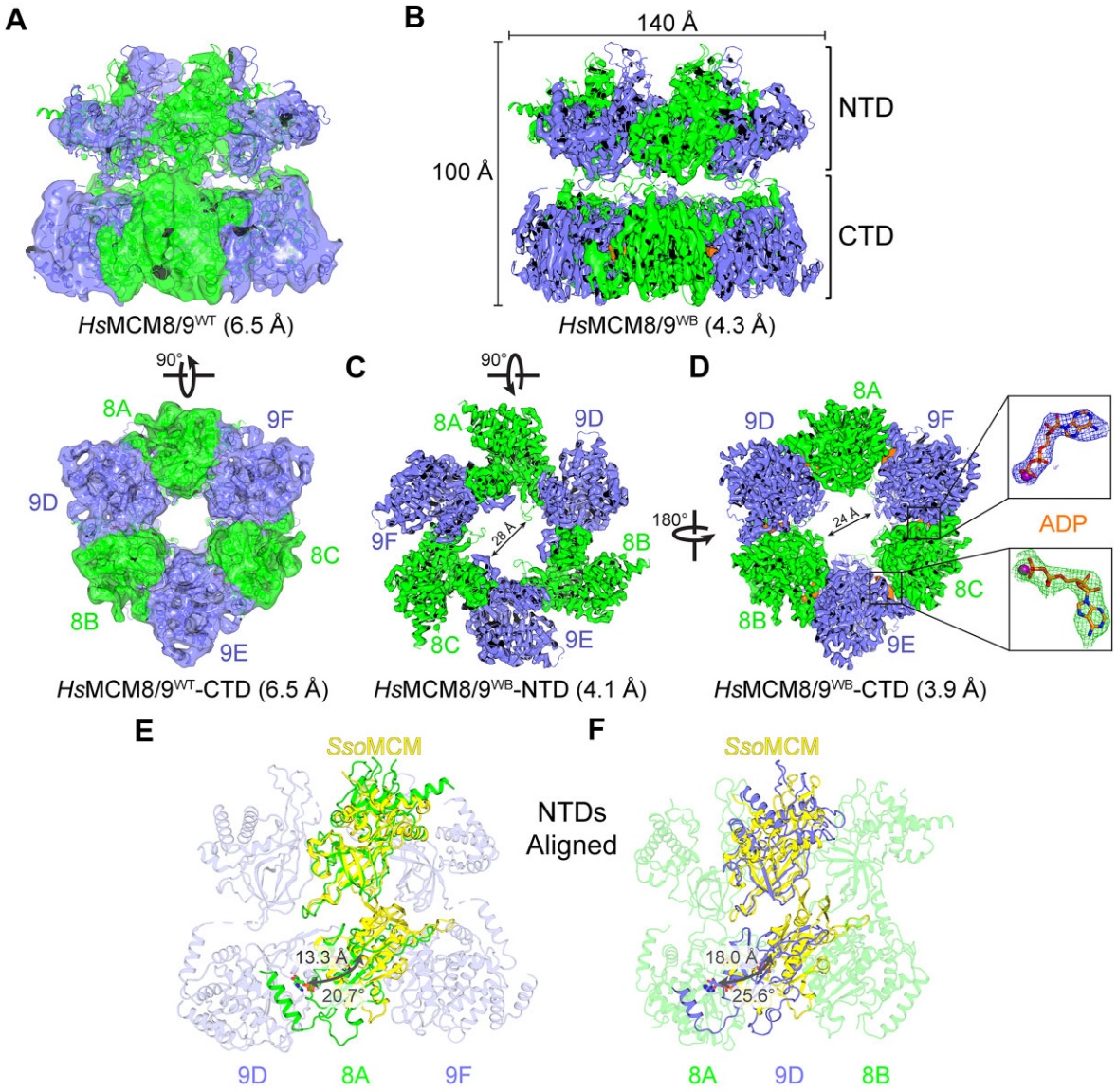

Figure 4. Overall heterohexamer cryo-EM structures of *Hs*MCM8/9 complexes. (**A**) Structure of *Hs*MCM8/9^{WT} with ATPγS at 6.5 Å. Side view (top) and the view along the central channel from the CTD (bottom). *Hs*MCM8 and *Hs*MCM9 are colored green and purple, respectively. (**B**) Structure of *Hs*MCM8/9^{WB} complex in the presence of ADP at 4.3 Å, with locally refined NTD (4.1 Å) and CTD (3.9 Å) shown in (**C**) and (**D**), respectively. ADP is shown in orange and Mg^{2+} in magenta. Cryo-EM density map for ADP in the ATPase sites at two different interfaces between *Hs*MCM8 and *Hs*MCM9 is shown in mesh in the zoomed-in boxes. CTD movement in (**E**) *Hs*MCM8 and in F) *Hs*MCM9 compared to *Sso*MCM when their NTD are aligned. To clearly demonstrate the domain movement, the *Hs*MCM8 and *Hs*MCM9 monomers in the center are in opaque and their CTD are partially shown.

ssDNA and ATP analogs (Figure 5E, F), which were captured in different ATP hydrolysis states (37). Our structure aligns well with the nucleotide bound *Sso*MCM, but not the apo form (Supplementary Figure S10). The ps1β DNA binding loop in MCM8 adopts a different conformation compared to that in *Sso*MCM, likely due to the absence of DNA. The allosteric communication loop (ACL) in the NTD of *Sso*MCM contacts the DNA binding loop h2i and ps1β from the CTD in the *Sso*MCM structure without DNA (38) and stays in close proximity (∼4 Å) for potential interactions in the structure with DNA (37). Furthermore, mutations on the ACL loops that disrupt this interaction eliminates *Sso*MCM translocation (41). Because of the relative movement between the CTD and NTD, contacts between ACL and the DNA binding loops, h2i and ps1β, are reduced in MCM8/9^{WB} (Figure 5E, F). Both h2i loops for MCM8 and 9 are unresolved in this structure likely from the lack of DNA binding.

Interestingly, ADP was observed at each ATPase site, consistent with biochemical assays that the ATPase activity was not completely abolished with the WB mutant. Additional densities can be found next to the phosphate group of ADP. Considering its location relative to the negatively charged ADP and protein sidechains and the similarities to other ATPase high-resolution structures, the density is tentatively assigned as Mg^{2+}. Similar to *Sso*MCM and eukaryotic MCM2–7, conserved motifs are found in MCM8/9 to support nucleotide binding and hydrolysis (37,42)

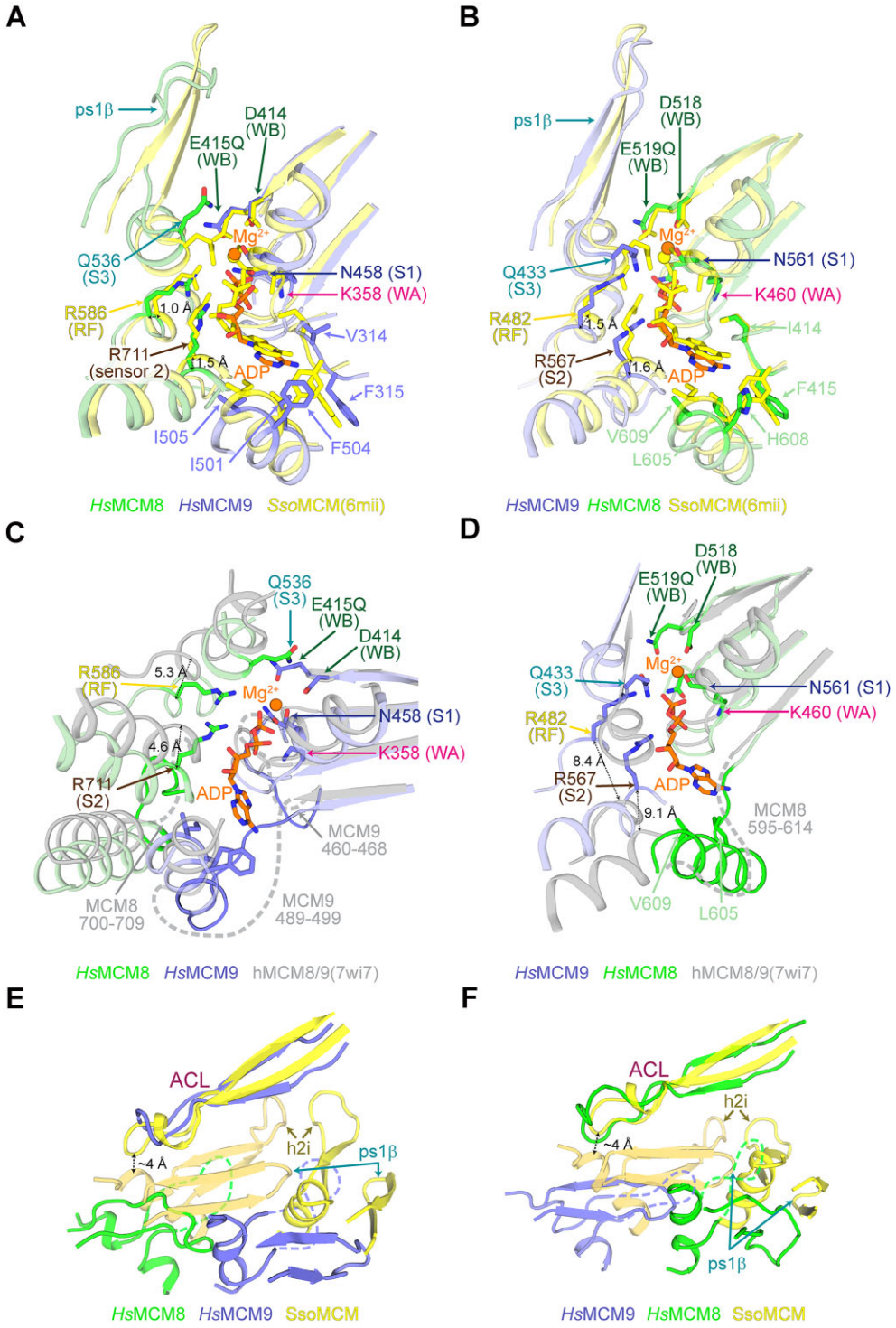

Figure 5. ATPase sites in *Hs*MCM8/9/ADP complex. Comparison of the ATPase sites (**A**) *Hs*MCM8-*Hs*MCM9 or (**B**) *Hs*MCM9-*Hs*MCM8 interfaces within the *Hs*MCM8/9^{WB} cryo-EM structure with that in *Sso*MCM hexamer in the ADP-type state (yellow, PDB ID, 6mii). ADP and Mg^{2+} are colored orange in *Hs*MCM8/9^{WB} cryo-EM structure and yellow in *Sso*MCM structure. Critical residues that form the arginine finger, Walker A and Walker B motifs, Sensor 1–3, and the hydrophobic pocket for accommodating ADP adenine ring are in stick. Cα shift of the arginine finger and sensor 2 residue is labeled. Comparison of the ATPase sites (**C**) *Hs*MCM8-*Hs*MCM9 or (**D**) *Hs*MCM9-*Hs*MCM8 in *Hs*MCM8/9^{WB} cryo-EM structure with that in the apo *Hs*MCM8/9 crystal structure (grey, PDB ID, 7wi7). Missing residues in the apo structure are shown as dashed (grey) lines and are highlighted in opaque in the cryo-EM structure. Diminished interaction between the ACL and h2i and ps1β in (**E**) *Hs*MCM8-*Hs*MCM9 or (**F**) *Hs*MCM9-*Hs*MCM8 interfaces within the *Hs*MCM8/9^{WB} complex compared to *Sso*MCM (shades of yellow). Parts of the ACL in *Hs*MCM9 and the h2i in *Hs*MCM8/9^{WB} is shown in dashed lines due to the absence of its electron density in the cryo-EM structure.

(Figure 5A-B). The WA motif (K358 on MCM9 or K460 on MCM8) wraps around the phosphate groups of the ADP; the WB motif (D414 and E415Q on MCM9 or D518 and E519Q on MCM8) stays in proximity to the Mg^{2+} for nucleophilic attack. Hydrophobic pockets formed by V314, F315, I501, F504 and I505 on MCM9 or I414, F415, L605, H608 and V609 on MCM8 are used to accommodate the adenosine base. On the other subunit, sensor 2 (R711 on MCM8 or R567 on MCM9) interacts with the β-phosphate, while the arginine finger (R586 on MCM8 or R482 on MCM9) does not strongly engage with ADP binding from the lack of the **γ**-phosphate. The ATPase sites at MCM8/9 and MCM9/8 interfaces are similar, with Mg^{2+} closer to the WB motif but farther from the ADP molecule in the latter (Supplementary Figure S10).

DISCUSSION

The biochemical properties for efficient DNA binding and unwinding and the structural features of the human MCM8/9 heterohexameric complex bound to ADP are described. Similar to MCM2–7, MCM8/9 has a high affinity binding (low nM K_d) for ssDNA in the presence of a nucleotide analogue that contains a gamma phosphate (43,44). However, MCM8/9 has low affinity for dsDNA or in the absence of any nucleotide as seen with other hexameric helicases (45). Interestingly, nuclease footprinting showed that MCM8/9 requires slowly hydrolyzable nucleoside triphosphates for stable loading onto the ssDNA portion of a fork substrate. When hydrolysis of ATP is possible or with addition of the product ADP, the stability of the bound MCM8/9 complex on DNA becomes weaker. Similar to other helicases (46), DNA stimulates the already robust ATP hydrolysis of MCM8/9. More efficient biochemical DNA unwinding requires sufficient length ssDNA on the 3′-arm and nucleoside triphosphates for stable loading of MCM8/9 prior to initiating with excess ATP. However, the total fraction unwound is not complete, indicating that we have not yet identified the ideal substrate, conditions, or activator proteins for MCM8/9 or that nonproductive binding of the helicase may be occurring on these substrates, as we have found previously for *Sso*MCM (47), requiring further examination. Altogether, this suggests that the ATPase cycle is coupled with states of high and low DNA binding affinities that influence coordination of the ACL and the h2i and ps1β loops needed to engage ssDNA and facilitate translocation for effective unwinding. It is also likely that interacting proteins such as HROB (23,25), stimulate MCM8/9 unwinding by reducing the residence time of the low affinity state, enforcing a more productive DNA unwinding conformation, possibly by constraining the CTD swing.

Similar to other MCM proteins, MCM8/9 forms stable hexameric rings with DNA binding loops in the central channel and active sites at each of subunit interface. However, this is the first example of a heterohexameric complex with a repeating heterodimer of trimers configuration. The ATP binding sites within the AAA^+ CTD are formed by two types of neighboring dimers (8 to 9 or 9 to 8), instead of one for *Sso*MCM or six with MCM2–7, with conserved motifs from each subunit. Interestingly, the combined single MCM8 and MCM9 WB (E to Q) mutants still showed a low-level of ATP hydrolysis leaving the product, ADP, bound in the active site of this structure. Likely, these mutations did not completely abrogate the ATPase activity, similar to that found for MCM2–7, where the single WB mutants proved to be non-lethal (44), and the preceding acidic aspartate can be responsible for activating ATP hydrolysis. As the ADP bound state of MCM8/9 has lower affinity for ssDNA, this may explain the absence of DNA in the cryo-EM structure. Although ATP**γ**S stabilizes MCM8/9 loading onto ssDNA, unwinding with ATP initiation is still limited to around 40%, suggesting that alternative loaded nonproductive complexes may exist. We also suspect that ssDNA may only engage strongly with the NTDs but not with the more flexible CTDs, and thus dissociate from MCM8/9 during grid preparation. Additional protein partners and/or post-translational modifications are possibly needed to promote DNA capture of MCM8/9 for structural investigations.

Structural analysis and comparison to *Sso*MCM structures support the assignment of the ADP bound state in the present $MCM8/9^{WB}$ structure. Surprisingly, the $MCM8/9^{WB}$ structure bound with ADP and the $MCM8/9^{WT}$ structure bound with ATP**γ**S adopt similar global conformations in the absence of DNA. In contrast, large scale conformational rearrangements of the ATP binding site and inter-subunit motions are observed when this ADP bound $MCM8/9^{WB}$ structure is compared to the apo *Hs*MCM8/9 crystal structure (40), indicating that nucleotide binding may be sufficient to shift the CTD. As proposed for other hexameric helicases, the CTD movement upon nucleotide binding may correlate with the sequential subunit translocation during DNA unwinding (48). Moreover, the large apparent swing between the NTD and the CTD, compared to *Sso*MCM, may indicate that MCM8/9 has a more difficult time engaging ssDNA in a proper orientation for effective ATPase-coupled translocation. It is intriguing that HROB has been shown to activate MCM8/9 unwinding (23,25), likely altering the CTD position for DNA capture and more active unwinding. To more completely decipher the MCM8/9 unwinding mechanism, it will be essential to obtain structures of the complex at each state of ATP hydrolysis and with DNA bound in the central channel to reveal the organization of the ACL, h2i, and ps1β loops for sequential subunit engagement of ssDNA during translocation. Moreover, revealing the precise interaction site for HROB (or other interacting proteins, such as MRE11 (20)) and how it structurally alters the heterohexameric structure will also be essential in better understanding the regulation of unwinding activity for this unique helicase.

DATA AVAILABILITY

The cryo-EM density maps for $MCM8/9^{WT}$ complexed with ATP**γ**S, the overall structure, NTD, and CTD of $MCM8/9^{WB}$ complexed with ADP have been deposited in the Electron Microscopy Data Bank under accession numbers EMD-40237, EMD-40234, EMD-40235, and EMD-40236, respectively. The atomic coordinates for the overall structure, NTD, and CTD of $MCM8/9^{WB}$ complexed with

ADP have been deposited in the Protein Data Bank under accession numbers PDB ID 8S91, PDB ID 8S92 and PDB ID 8S94. The authors confirm that all other relevant data are present in the manuscript and its supplementary data. Materials in this study are available from the corresponding author upon reasonable request.

SUPPLEMENTARY DATA

Supplementary Data are available at NAR Online.

ACKNOWLEDGEMENTS

The authors wish to thank the Molecular Biosciences Center at Baylor University for access to equipment and to Dr. Jung-Hyun Min for use of the homogenizer. We thank the cryo-EM core facilities at Baylor College of Medicine and University of Texas McGovern Medical School, both of which are supported by CPRIT RP190602, for sample screening and data collection.
Author contributions: D.R.M. purified MCM8/9 proteins, performed all of the *in vitro* biochemical assays including DNA binding, ATPase, S1 protection, and DNA unwinding. C.L. prepared the frozen grids and performed all of the cryo-EM analysis. Y.G. supervised C.L. and provided support and expertise on the cryo-EM analysis. M.A.T. conceived and supervised the entire project and wrote the manuscript with input from all the authors.

FUNDING

This work was supported by Baylor University; the National Institutes of Health [GM13791 to M.A.T.]; Cancer Prevention & Research Institute of Texas (CPRIT) Award [RR190046 to Y.G.]; and American Cancer Society Research Scholar award [RSG-22-082-01-DMC to Y.G.]. Funding for open access charge: Baylor University.
Conflict of interest statement. None declared.

REFERENCES

1. Duderstadt,K.E. and Berger,J.M. (2008) AAA$^+$ ATPases in the initiation of DNA replication. *Crit. Rev. Biochem. Mol. Biol.*, **43**, 163–187.
2. Erzberger,J.P. and Berger,J.M. (2006) Evolutionary relationships and structural mechanisms of AAA$^+$ proteins. *Annu. Rev. Biophys. Biomol. Struct.*, **35**, 93–114.
3. Iyer,L.M., Leipe,D.D., Koonin,E.V. and Aravind,L. (2004) Evolutionary history and higher order classification of AAA$^+$ ATPases. *J. Struct. Biol.*, **146**, 11–31.
4. Tarsounas,M. and Sung,P. (2020) The antitumorigenic roles of BRCA1-BARD1 in DNA repair and replication. *Nat. Rev. Mol. Cell Biol.*, **21**, 284–299.
5. Graham,B.W., Schauer,G.D., Leuba,S.H. and Trakselis,M.A. (2011) Steric exclusion and wrapping of the excluded DNA strand occurs along discrete external binding paths during MCM helicase unwinding. *Nucleic Acids Res.*, **39**, 6585–6595.
6. Nishimura,K., Ishiai,M., Horikawa,K., Fukagawa,T., Takata,M., Takisawa,H. and Kanemaki,M.T. (2012) Mcm8 and Mcm9 form a complex that functions in homologous recombination repair induced by DNA interstrand crosslinks. *Mol. Cell*, **47**, 511–522.
7. Jeffries,E.P., Denq,W.I., Bartko,J.C. and Trakselis,M.A. (2013) Identification, quantification, and evolutionary analysis of a novel isoform of MCM9. *Gene*, **519**, 41–49.
8. Liu,Y., Richards,T.A. and Aves,S.J. (2009) Ancient diversification of eukaryotic MCM DNA replication proteins. *BMC. Evol. Biol.*, **9**, 60.
9. Gozuacik,D., Chami,M., Lagorce,D., Faivre,J., Murakami,Y., Poch,O., Biermann,E., Knippers,R., Brechot,C. and Paterlini-Brechot,P. (2003) Identification and functional characterization of a new member of the human Mcm protein family: hMcm8. *Nucleic Acids Res.*, **31**, 570–579.
10. Lutzmann,M., Maiorano,D. and Mechali,M. (2005) Identification of full genes and proteins of MCM9, a novel, vertebrate-specific member of the MCM2-8 protein family. *Gene*, **362**, 51–56.
11. Yoshida,K. (2005) Identification of a novel cell-cycle-induced MCM family protein MCM9. *Biochem. Biophys. Res. Commun.*, **331**, 669–674.
12. Fauchereau,F., Shalev,S., Chervinsky,E., Beck-Fruchter,R., Legois,B., Fellous,M., Caburet,S. and Veitia,R.A. (2016) A non-sense MCM9 mutation in a familial case of primary ovarian insufficiency. *Clin. Genet.*, **89**, 603–607.
13. Wood-Trageser,M.A., Gurbuz,F., Yatsenko,S.A., Jeffries,E.P., Kotan,L.D., Surti,U., Ketterer,D.M., Matic,J., Chipkin,J., Jiang,H. *et al.* (2014) MCM9 mutations are associated with ovarian failure, short stature, and chromosomal instability. *Am. J. Hum. Genet.*, **95**, 754–762.
14. AlAsiri,S., Basit,S., Wood-Trageser,M.A., Yatsenko,S.A., Jeffries,E.P., Surti,U., Ketterer,D.M., Afzal,S., Ramzan,K., Faiyaz-Ul Haque,M. *et al.* (2015) Exome sequencing reveals MCM8 mutation underlies ovarian failure and chromosomal instability. *J. Clin. Invest.*, **125**, 258–262.
15. Alvarez-Mora,M.I., Todeschini,A.L., Caburet,S., Perets,L.P., Mila,M., Younis,J.S., Shalev,S. and Veitia,R.A. (2020) An exome-wide exploration of cases of primary ovarian insufficiency uncovers novel sequence variants and candidate genes. *Clin. Genet.*, **98**, 293–298.
16. Franca,M.M., Funari,M.F.A., Lerario,A.M., Santos,M.G., Nishi,M.Y., Domenice,S., Moraes,D.R., Costalonga,E.F., Maciel,G.A.R., Maciel-Guerra,A.T. *et al.* (2020) Screening of targeted panel genes in Brazilian patients with primary ovarian insufficiency. *PLoS One*, **15**, e0240795.
17. Kherraf,Z.E., Cazin,C., Bouker,A., Fourati Ben Mustapha,S., Hennebicq,S., Septier,A., Coutton,C., Raymond,L., Nouchy,M., Thierry-Mieg,N. *et al.* (2022) Whole-exome sequencing improves the diagnosis and care of men with non-obstructive azoospermia. *Am. J. Hum. Genet.*, **109**, 508–517.
18. Tenenbaum-Rakover,Y., Weinberg-Shukron,A., Renbaum,P., Lobel,O., Eideh,H., Gulsuner,S., Dahary,D., Abu-Rayyan,A., Kanaan,M., Levy-Lahad,E. *et al.* (2015) Minichromosome maintenance complex component 8 (MCM8) gene mutations result in primary gonadal failure. *J. Med. Genet.*, **52**, 391–399.
19. McKinzey,D.R., Gomathinayagam,S., Griffin,W.C., Klinzing,K.N., Jeffries,E.P., Rajkovic,A. and Trakselis,M.A. (2021) Motifs of the C-terminal domain of MCM9 direct localization to sites of mitomycin-C damage for RAD51 recruitment. *J. Biol. Chem.*, **296**, 100355.
20. Lee,K.Y., Im,J.S., Shibata,E., Park,J., Handa,N., Kowalczykowski,S.C. and Dutta,A. (2015) MCM8-9 complex promotes resection of double-strand break ends by MRE11-RAD50-NBS1 complex. *Nat. Commun.*, **6**, 7744.
21. Griffin,W.C., McKinzey,D.R., Klinzing,K.N., Baratam,R., Eliyapura,A. and Trakselis,M.A. (2022) A multi-functional role for the MCM8/9 helicase complex in maintaining fork integrity during replication stress. *Nat. Commun.*, **13**, 5090.
22. Morii,I., Iwabuchi,Y., Mori,S., Suekuni,M., Natsume,T., Yoshida,K., Sugimoto,N., Kanemaki,M.T. and Fujita,M. (2019) Inhibiting the MCM8-9 complex selectively sensitizes cancer cells to cisplatin and olaparib. *Cancer Sci.*, **110**, 1044–1053.
23. Hustedt,N., Saito,Y., Zimmermann,M., Alvarez-Quilon,A., Setiaputra,D., Adam,S., McEwan,A., Yuan,J.Y., Olivieri,M., Zhao,Y. *et al.* (2019) Control of homologous recombination by the HROB-MCM8-MCM9 pathway. *Genes Dev.*, **33**, 1397–1415.
24. Wang,C., Chen,Z., Su,D., Tang,M., Nie,L., Zhang,H., Feng,X., Wang,R., Shen,X., Srivastava,M. *et al.* (2020) C17orf53 is identified as a novel gene involved in inter-strand crosslink repair. *DNA Repair (Amst.)*, **95**, 102946.
25. Huang,J.W., Acharya,A., Taglialatela,A., Nambiar,T.S., Cuella-Martin,R., Leuzzi,G., Hayward,S.B., Joseph,S.A., Brunette,G.J., Anand,R. *et al.* (2020) MCM8IP activates the MCM8-9 helicase to promote DNA synthesis and homologous recombination upon DNA damage. *Nat. Commun.*, **11**, 2948.

26. Li,J., Yu,D., Liu,L., Liang,H., Ouyang,Q. and Liu,Y. (2021) Structural study of the N-terminal domain of human MCM8/9 complex. *Structure*, **29**, 1171–1181.
27. Scholz,J. and Suppmann,S. (2017) A new single-step protocol for rapid baculovirus-driven protein production in insect cells. *BMC Biotechnol.*, **17**, 83.
28. Zheng,S.Q., Palovcak,E., Armache,J.P., Verba,K.A., Cheng,Y. and Agard,D.A. (2017) MotionCor2: anisotropic correction of beam-induced motion for improved cryo-electron microscopy. *Nat. Methods*, **14**, 331–332.
29. Zhang,K. (2016) Gctf: real-time CTF determination and correction. *J. Struct. Biol.*, **193**, 1–12.
30. Zivanov,J., Nakane,T., Forsberg,B.O., Kimanius,D., Hagen,W.J., Lindahl,E. and Scheres,S.H. (2018) New tools for automated high-resolution cryo-EM structure determination in RELION-3. *Elife*, **7**, e42166.
31. Punjani,A., Rubinstein,J.L., Fleet,D.J. and Brubaker,M.A. (2017) cryoSPARC: algorithms for rapid unsupervised cryo-EM structure determination. *Nat. Methods*, **14**, 290–296.
32. Pettersen,E.F., Goddard,T.D., Huang,C.C., Couch,G.S., Greenblatt,D.M., Meng,E.C. and Ferrin,T.E. (2004) UCSF Chimera–a visualization system for exploratory research and analysis. *J. Comput. Chem.*, **25**, 1605–1612.
33. Emsley,P., Lohkamp,B., Scott,W.G. and Cowtan,K. (2010) Features and development of Coot. *Acta Crystallogr. D Biol. Crystallogr.*, **66**, 486–501.
34. Afonine,P.V., Poon,B.K., Read,R.J., Sobolev,O.V., Terwilliger,T.C., Urzhumtsev,A. and Adams,P.D. (2018) Real-space refinement in PHENIX for cryo-EM and crystallography. *Acta Crystallogr. D Struct. Biol.*, **74**, 531–544.
35. Griffin,W.C. and Trakselis,M.A. (2019) The MCM8/9 complex: a recent recruit to the roster of helicases involved in genome maintenance. *DNA Repair (Amst.)*, **76**, 1–10.
36. Gao,Y., Cui,Y., Fox,T., Lin,S., Wang,H., de Val,N., Zhou,Z.H. and Yang,W. (2019) Structures and operating principles of the replisome. *Science*, **363**, eaav7003.
37. Meagher,M., Epling,L.B. and Enemark,E.J. (2019) DNA translocation mechanism of the MCM complex and implications for replication initiation. *Nat. Commun.*, **10**, 3117.
38. Miller,J.M., Arachea,B.T., Epling,L.B. and Enemark,E.J. (2014) Analysis of the crystal structure of an active MCM hexamer. *Elife*, **3**, e03433.
39. Yuan,Z., Bai,L., Sun,J., Georgescu,R., Liu,J., O'Donnell,M.E. and Li,H. (2016) Structure of the eukaryotic replicative CMG helicase suggests a pumpjack motion for translocation. *Nat. Struct. Mol. Biol.*, **23**, 217–224.
40. Weng,Z., Zheng,J., Zhou,Y., Wu,Y., Xu,D., Li,H., Liang,H. and Liu,Y. (2023) Structural and mechanistic insights into the MCM8/9 helicase complex. *eLife*, **12**, RP87468.
41. Barry,E.R., Lovett,J.E., Costa,A., Lea,S.M. and Bell,S.D. (2009) Intersubunit allosteric communication mediated by a conserved loop in the MCM helicase. *Proc. Natl. Acad. Sci. U. S. A.*, **106**, 1051–1056.
42. Yuan,Z., Georgescu,R., Bai,L., Zhang,D., Li,H. and O'Donnell,M.E. (2020) DNA unwinding mechanism of a eukaryotic replicative CMG helicase. *Nat. Commun.*, **11**, 688.
43. Patel,S.S. and Picha,K.M. (2000) Structure and function of hexameric helicases. *Annu. Rev. Biochem.*, **69**, 651–697.
44. Bochman,M.L. and Schwacha,A. (2007) Differences in the single-stranded DNA binding activities of MCM2–7 and MCM467: MCM2 and MCM5 define a slow ATP-dependent step. *J. Biol. Chem.*, **282**, 33795–33804.
45. Onwubiko,N.O., Borst,A., Diaz,S.A., Passkowski,K., Scheffel,F., Tessmer,I. and Nasheuer,H.P. (2020) SV40 T antigen interactions with ssDNA and replication protein A: a regulatory role of T antigen monomers in lagging strand DNA replication. *Nucleic Acids Res.*, **48**, 3657–3677.
46. Bochman,M.L. and Schwacha,A. (2009) The Mcm complex: unwinding the mechanism of a replicative helicase. *Microbiol. Mol. Biol. Rev.*, **73**, 652–683.
47. Perera,H.M. and Trakselis,M.A. (2019) Amidst multiple binding orientations on fork DNA, *Saccharolobus* MCM helicase proceeds N-first for unwinding. *Elife*, **8**, e46096.
48. Gao,Y. and Yang,W. (2020) Different mechanisms for translocation by monomeric and hexameric helicases. *Curr. Opin. Struct. Biol.*, **61**, 25–32.